



## Full Length Article

# Comparison of three nanoparticle deposition techniques potentially applicable to elemental mapping by nanoparticle-enhanced laser-induced breakdown spectroscopy

F.A. Casian-Plaza<sup>a,b</sup>, P.M. Janovszky<sup>a</sup>, D.J. Palásti<sup>a,b</sup>, A. Kohut<sup>c</sup>, Zs. Geretovszky<sup>c</sup>, J. Kopniczky<sup>c</sup>, F. Schubert<sup>d</sup>, S. Živković<sup>e</sup>, Z. Galbács<sup>a</sup>, G. Galbács<sup>a,b,\*</sup>

<sup>a</sup> Department of Molecular and Analytical Chemistry, University of Szeged, Dóm square 7-8, 6720 Szeged, Hungary

<sup>b</sup> HUN-REN Wigner Research Centre for Physics, P.O.Box 49., 1525 Budapest, Hungary

<sup>c</sup> Department of Optics and Quantum Electronics, University of Szeged, Dóm square 9, 6720 Szeged, Hungary

<sup>d</sup> Department of Mineralogy, Geochemistry and Petrology, University of Szeged, Egyetem street 2, 6722 Szeged, Hungary

<sup>e</sup> Vinča Institute of Nuclear Sciences, University of Belgrade, P.O. Box 522, 11001 Belgrade, Serbia

## ARTICLE INFO

## Keywords:

Spray coating  
Magnetron sputtering  
Spark discharge nanoparticle generation  
Thermal annealing  
Nanoparticle-enhanced laser-induced breakdown spectroscopy (NE-LIBS)

## ABSTRACT

In this study, we compared the applicability of three nanoparticle deposition techniques (spray coating, spark discharge nanoparticle generation, magnetron sputtering) towards elemental mapping by nanoparticle-enhanced laser-induced breakdown spectroscopy (NE-LIBS). It was found that sputtering followed by a thermal treatment at 550 °C can provide a homogenous, practical and controllable way of NE-LIBS sample preparation with gold nanoparticles. The laser ablation properties of the created NP layer was also studied in detail and it was established that a 200 µm laser spot size is good compromise between the NE-LIBS signal enhancement and the spatial resolution required for mapping. A signal enhancement of about a factor of 10 with good repeatability (ca. 5 %RSD) in a line scanning demonstration was achieved on glass for Si detection. For samples that are fairly temperature and vacuum stable, this approach allows the signal enhancement to be used in mapping applications.

## 1. Introduction

Laser-induced breakdown spectroscopy (LIBS) is becoming a more and more popular analytical method suitable for the sensitive, direct investigation of solids (surfaces). Its popularity in science and industry is due to a combination of advantageous analytical properties. These include fast localized analysis (e.g. in less than a second), trace analytical (ppm or µg·g<sup>-1</sup> level) limits of detection (LODs), little to no sample preparation, contactless (or even stand-off) operation, and a true hyperspectral approach [1–3]. The recorded single-shot, high resolution spectra contain a large amount of chemical information, which not only provides quantitative analytical information about all elements, or indirectly about isotopic and molecular components of the sample [4], but the spectra can also be used as a highly characteristic profile (“spectral fingerprint”) based on which the (local) sample quality can be compared, identified or classified. The lateral resolution of LIBS analysis is typically in the 20–50 µm range, but sub-micron resolutions have also

been demonstrated to be achievable. By taking advantage of the ablative property of the focused laser beam, depth-resolved analysis is also possible with a resolution also at the micrometer level [5,6]. Detailed descriptions of LIBS can be found in recent general reviews (e.g. [1–3]) and books (e.g. [6–12]) dedicated to this method.

As with all laser spectroscopy methods, where the spatial resolution of the measurement is also related to the LODs, there is an ongoing quest for the improvement of the limits of detection in LIBS, too. To this end, an array of techniques and approaches with varying practicality (e.g. the use of double or multiple laser pulses, plasma confinement or reheating using external sources of energy, etc.) have been proposed and tested already [1,13,14]. The nanoparticle-enhanced LIBS (NE-LIBS) is an approach that can offer both a large signal enhancement, sometimes as large as two orders of magnitude, and practicality, as it only requires the deposition and drying of a plasmonic metal (e.g. gold) nanoparticle (NP) dispersion on the solid sample prior to LIBS analysis [15,16]. Over the years, detailed studies have been performed, mainly by de Giacomo’s

\* Corresponding author at: Department of Molecular and Analytical Chemistry, University of Szeged, Dóm square 7-8, 6720 Szeged, Hungary.

E-mail address: [galbx@chem.u-szeged.hu](mailto:galbx@chem.u-szeged.hu) (G. Galbács).

<https://doi.org/10.1016/j.apsusc.2024.159844>

Received 16 January 2024; Received in revised form 1 March 2024; Accepted 4 March 2024

Available online 5 March 2024

0169-4332/© 2024 The Authors. Published by Elsevier B.V. This is an open access article under the CC BY license (<http://creativecommons.org/licenses/by/4.0/>).

group in Italy and his collaborators, with the intention to shed light on the mechanisms behind the NE-LIBS signal enhancement as well as the influence of experimental conditions [17–19].

It was revealed that metallic NPs mediate the optical breakdown of solid surfaces, more closely promote the production of free electrons (seed electrons) needed for plasma induction, which are otherwise typically generated by the multiphoton ionization mechanism. In the presence of metallic NPs, localized surface plasmons (LSPs) induced within the NPs can enhance the electromagnetic field of the incident radiation and generate additional electrons via field emission. Since field enhancement is produced on multiple NPs simultaneously, several electron extraction points are available in the laser spot, leading to multiple plasma ignition points (this also changes the appearance of ablation craters). The efficient coupling of LSPs requires the NPs to be deposited in close vicinity to each other. The resonance of the laser wavelength with particle dimensions can also promote the phenomenon [20]. These effects are most enhanced in electrically conducting solids [16]. Metallic samples were found to give rise to the largest NE-LIBS signal enhancement (e.g. 10–100-fold), whereas the effect is generally modest for semiconducting or insulating solid samples (e.g. a factor of a few). The surface concentration of NPs, as well as laser fluence was also found to play an important role and the optimal conditions were established [17,18]. In addition to the classical droplet deposition technique, e.g. electrochemical deposition [21], magnetron sputtering [22] and pulsed laser ablation in liquid [23] was also tested for localized NE-LIBS analysis. Please note that the nanoparticle-induced signal enhancement affects the intensity of all spectral features in the LIBS spectrum (atomic lines, ionic lines, molecular bands, etc.), however the actual value of signal enhancement is different for different spectral features – in this aspect, NE-LIBS is similar to surface enhanced Raman spectroscopy.

One of the analytical application areas in which LIBS excels in recent years is elemental mapping. LIBS has been tested and tried for diverse sample types in many quantitative and qualitative analytical scenarios ranging from forensic science over materials science, biology, geology to medical diagnostics [5,6,24–28]. The reason of LIBS's popularity in this field is that it provides a true hyperspectral approach with trace analytical sensitivity [24,29]. The provided, typically 10–50  $\mu\text{m}$  range, spatial resolution is not as good as for some other chemical mapping methods (e.g. laser ablation inductively coupled plasma mass spectrometry, LA-ICP-MS, or synchrotron  $\mu\text{-X}$ -ray fluorescence spectroscopy,  $\mu\text{-XRF}$ ), but can be utilized in a wide range of applications and for all elements, moreover it suffers from less interferences (e.g. related to material transport, as in LA-ICP-MS). LIBS also provides good single-shot performance. Taking advantage of the ablative character of LIBS, layer-by-layer depth-resolved mapping is also possible for depths of up to a few hundred micrometers [5].

The adaptation of the nanoparticle enhancement approach is attractive also for LIBS mapping. Indeed, most recently, a couple of research groups have reported about the successful use of the NE-LIBS approach for mapping in e.g. metallic [30] and plant samples [31]. It is also worth mentioning that capitalizing on the similarities in the ablation process, nanoparticle enhanced LA-ICP-MS (NE-LA-ICP-MS) has also been tested for some sample types, with varying success [32–34]. However, along with the accumulation of experiences, some challenges also came to light and some realizations were made. Of these, the primary one is that a very homogeneous deposition of plasmonic metal NPs should be applied to the solid surface, as the usual droplet deposition, which works well for localized NE-LIBS analysis, produces an uncontrolled and uneven distribution of nanoparticles (aggregation, „coffee-ring“ shapes, etc.) [10]. A very even distribution of (highly similar) NPs is an essential requirement for mapping, as the signal enhancement factor must be as similar in each analytical spot as possible in order to retain the chemical information (at least it should only be influenced by the local material quality of the sample). In addition, the simple droplet deposition approach obviously is also incapable of

covering larger areas (e.g. several  $\text{cm}^2$ ), which are required in many analytical mapping situations. In spite of this, the couple of NE-LIBS mapping studies conducted so far have resorted to the use of droplet deposition. Another challenge associated with NE-LIBS mapping comes from that the theory stipulates that a large laser spot size to be used, which facilitates the coupling of as many as possible localized surface plasmons for a larger effect. It is therefore not uncommon in localized NE-LIBS to use analytical spot sizes as large as 2 mm in diameter, which also helps to cover up (average over) the uneven surface concentration of NPs within the spot [35]. However, the requirement of a (too) large spot size is obviously directly against the general interest of chemical mapping, as it imposes a limitation on the spatial resolution, thereby even eliminating certain applications (e.g. granular rock analysis, bio-analysis with cell-resolution, etc.). Clearly, a compromise or optimum needs to be established in terms of laser spot size. The signal enhancement being dependent on the electrical conductivity (or transparency) of the sample, a well-described effect in most NE-LIBS or NE-LA-ICP-MS studies, is a characteristic that largely magnifies the matrix effects already existing in LIBS and LA-ICP-MS – the analyte signal is not only a function of the local concentration of the analyte in the sample, but also the laser-material interaction (even if all conditions, including those related to NP deposition, are constant). This makes the interpretation of intensity-scaled elemental maps difficult or sometimes unreliable. The problem is even more serious if one attempts to produce quantitative (concentration-scaled) elemental maps. In these situations, the use of a matrix-corrected calibration is unavoidable, which makes the analytical process far more difficult (e.g. [27,36,37]). Last, but not least, the optimization of the extent of signal enhancement, e.g. in terms of NP size, laser wavelength, gate delay and width, has to be done more carefully in NE-LIBS mapping, as many samples are one of a kind, thus the measurement can not be repeated. Not to mention that the (local) material quality dependence of the signal enhancement factor effectively makes the optimization relative anyway.

Since we felt that the above questions and challenges have not yet been addressed in the NE-LIBS literature adequately so far, we set out to investigate them in detail. In the present study, we scrutinize three alternative NP deposition techniques (spray coating, spark discharge, magnetron sputtering) and assessed their usefulness in NE-LIBS mapping in comparison with the droplet deposition approach. We also study the laser ablation behavior of the deposited NPs and the repeatability of the signal enhancement.

## 2. Materials and methods

### 2.1. Nanoparticle deposition

The deposition targets used were 10  $\times$  10 mm silicon wafer chips (Ted Pella, Inc., USA) and soda-lime glass microscope slides (Eppredia, Germany). Gold nanoparticles were deposited during the experiments using the following techniques: spray coating, spark discharge generation and sputtering. Sample manipulation was carried out under a vertical flow laminar cabinet (Alpine K700, Poland) providing a HEPA-filtered, dust-free environment. Details of the deposition processes are described below.

Spray coating was performed using spherical gold NPs with 30 nm diameter in a 0.05  $\text{mg}\cdot\text{mL}^{-1}$  concentration (Pelco NanoXact, Ted Pella, Inc., USA) onto silicon chips, employing a gravity-fed spray gun (DU-30 K, Aircraft, South Africa) with a 200  $\mu\text{m}$  orifice, using 3 bar argon gas for nebulization. Surface concentration was controlled by the spraying time and varied in the range of 10 to 100 s, with a constant working distance of 25 cm. Spraying was followed by a 60 s duration drying under an IR lamp.

Spark discharge generation-based NP deposition was carried out in our laboratory-built system. It consists of a DN-160 sized, cylindrical stainless-steel vacuum chamber equipped with KF-40 ports. The pair of cylindrical Au electrodes (99.9 % purity, Goodfellow Cambridge Ltd.,

UK) were horizontally positioned and axially aligned with a gap distance of 2.0 mm from each other. The generated particles leave the chamber via a port at the top of the chamber. Argon (99.996 % purity, Messer Hungarogáz Kft., Hungary) was employed as carrier gas and fed through a 2.85 mm inner diameter injector orifice, with its tip placed at the midpoint between the electrodes at a distance of 4.25 mm from the common axis of the two electrodes. The 5.0 L·min<sup>-1</sup> gas flow rate was set by using a mass flow controller (GFC16, Aalborg Inc, USA). Particle generation was carried out at atmospheric pressure monitored by a pressure gauge (VD81, Pfeiffer Vacuum GmbH/Thyracont Vacuum Instruments GmbH). Spark discharges were generated by a capacitor charging circuit (450PM980, General Atomics, USA) of 8 nF capacitance charged by a high voltage power supply (HCK 800–12500, FuG GmbH, Germany). The resulting spark discharge is a bipolar, oscillatory discharge. The repetition rate of sparking was kept constant at 100 Hz by controlling the charging current of the capacitor. The aerosol flow passed through a tube furnace (Carbolite Gero GmbH, Germany) set at 900 °C, where compaction of the nano-aggregates occurred. The nano-aerosol was directed onto the substrate (e.g. silicon chip) in a perpendicular direction by a low pressure inertial impactor. Deposition times used were varied and controlled by an on/off valve before the impactor. Further details of our spark discharge setup can be found in e.g. [38–40].

Magnetron sputtering deposition was performed using a Quorum Q150RS Plus (Quorum Technologies, UK) rotary-pumped coater, on glass microscope slides as substrates. Sputtering was accomplished from a high purity, 57 mm diameter, 0.1 mm thick gold target (99.99 %, Goodfellow Cambridge Ltd., UK). The target-substrate distance was 60 mm. We kept the current at 20 mA and the argon pressure at 0.1 mbar, while the substrate was rotated with a speed of 25 rpm. Sputtering time was varied in a range from 60 to 360 s. In some experiments, the deposited gold thin film was subjected to thermal treatment in a muffle furnace (Thermolyne 62700, USA) at 550 °C for 20 min. The treated samples were left to cool at room temperature. This thermal treatment methodology was taken from the literature [41,42] and resulted in changes of surface morphology and creation of “quasi-spherical” structures in the gold layer.

## 2.2. Nanoparticle and surface characterization

Size distribution of the gold nanoparticles on the surface resulting from the deposition techniques as well as their laser ablation behaviour were documented by scanning electron microscopy (SEM, S-4700, Hitachi, Japan) using an accelerating voltage of 10 kV and an electron beam current of 10 µA.

Determination of the total surface concentration (µg·cm<sup>-2</sup>) of the deposited gold was performed using an inductively coupled plasma mass spectrometer (ICP-MS, 7700x, Agilent Technologies, USA). Sample dissolution was achieved by aqua regia (prepared freshly from trace quality concentrated hydrochloric and nitric acids, VWR Chemicals, USA). The solutions were introduced by an integrated autosampler (I-AS) and a MicroMist pneumatic nebulizer equipped with a Peltier-cooled Scott spray chamber, using a sample uptake rate of 600 µL·min<sup>-1</sup>. The plasma and interface set up parameters were the following: RF forward power 1550 W, argon plasma gas flow rate 15.0 L·min<sup>-1</sup>, argon carrier gas flow rate 1.05 L·min<sup>-1</sup> and plasma sampling depth 10.0 mm. <sup>209</sup>Bi was employed as internal standard signal and the gold calibration curve was built in the range of 0 ppb – 100 ppb using standard stock solutions (Inorganic Ventures, USA). All analytical measurements were carried out by monitoring the signal of the <sup>197</sup>Au isotope.

## 2.3. LIBS measurements

All LIBS measurements were performed using a J200 LIBS/LA tandem instrument (Applied Spectra, USA) equipped with a Q-switched Nd:YAG laser source operating at 266 nm with a pulse duration of 6 ns. The

LIBS detection system consisted of a six-channel CCD spectrometer with a spectral coverage of 190 to 1040 nm and a resolution of 0.07 nm. The system was controlled by Applied Spectra's Axiom LA 2.4 operation software, typically employing a 0.5 µs gate delay and 1 ms gate width. Experiments were carried out under constant argon flow with a rate of 1 L·min<sup>-1</sup>. Most NE-LIBS scanning/mapping measurements were carried out employing stepwise scans with non-overlapping 200 µm spot sizes (in one experiment, we also used 60 µm spot size). The pulse energy applied was varied between 10 and 18 mJ, which corresponded to fluences of 31 to 56 J·cm<sup>-2</sup>.

## 2.4. Data evaluation

LIBS data processing and elemental map generation was primarily carried out in the ClarityNeXt 1.0 software (Applied Spectra, USA). SEM images were analyzed by the open source, Java-based ImageJ software in order to calculate the mean particle diameter and interparticle distances. All graphs were prepared in Origin 9.0 (OriginLabs, USA). Please note that all signal enhancements (SEs) in the study were calculated based on the net intensity of specific spectral features (e.g. the Si I 288.15 nm spectral line), according to the usual formula of  $SE = I_{\text{with NPs}}/I_{\text{without NPs}}$ .

## 3. Results and discussion

### 3.1. Comparison of the morphology of the deposited NP layers

The Au NP layers deposited by all three approaches were investigated using SEM to assess the homogeneity of the deposition, as well as to obtain information about the morphology and size distribution of the deposited particles.

Spray coating produced large, ringlike deposits, and within these patterns, NP aggregates with arbitrary shape and size were observed. The overall appearance of the deposited material is quite inhomogeneous at the microscopic level, as is illustrated in Fig. 1. The deposited shapes associated with the technique have been already reported in the literature [43,44]. It was established that these shapes usually form whenever the surface is partially wetted by the suspension medium. Solid particles dispersed in the medium migrate to the edge of the drop during drying and there they aggregate, thereby forming a solid ring consisting of inner “islands”. Experiments have shown that the migration is caused by an outward flow within the drop that is driven by the loss of solvent by evaporation [43,44]. Thus, although spray coating delivers thousands of microdroplets to the surface of the target, the deposited material is too inhomogeneously distributed for NE-LIBS mapping purposes.

Spark discharge generation produced a much more homogenous NP distribution across the substrate surface and did not extensively form aggregates. Fairly spherical nanoparticles were deposited generally individually on the target, which were separated by a more or less uniform gap. It has to be mentioned however that we tested two ways for the direction of the nanoaerosol flow onto the deposition target: via an orifice (focusing the stream into a narrow beam using a low inertia impactor) or directly (without focusing). As was predictable, the use of the orifice produces a more concentrated nanoaerosol beam, which creates a higher surface particle concentration in the center, but the concentration thins out towards the edge of the target. This radial concentration gradient is depicted in Fig. 2a. On the other hand, without the orifice the deposition is quite homogeneous across the whole surface of the target (Fig. 2b.). However, this comes with a significantly lower particle surface concentration than that achievable with the orifice, considering identical deposition times. With the increase of the deposition time, the size of occasional aggregates is also growing on the surface, but evenly. In other words, not a small number of very large aggregates are formed, but a large number of small aggregates. The mean particle size was found to be around 22 nm and it remained fairly



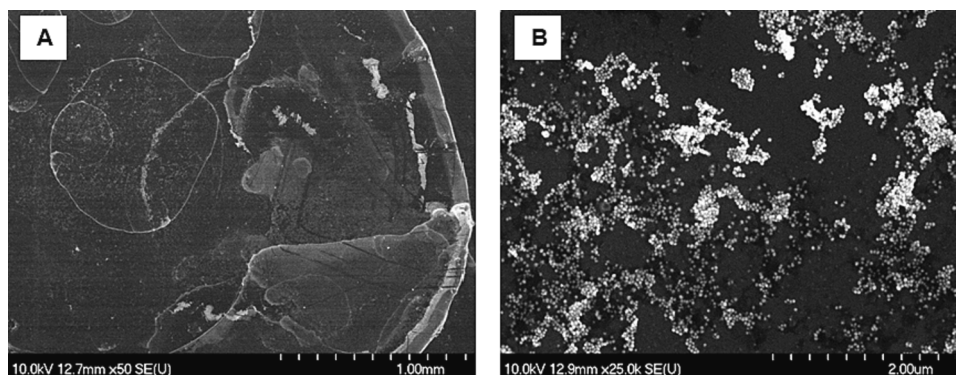


**Fig. 1.** SEM images of NP deposits generated by the spray coating technique. Images A and B were taken on different places on the substrate, with different magnifications.

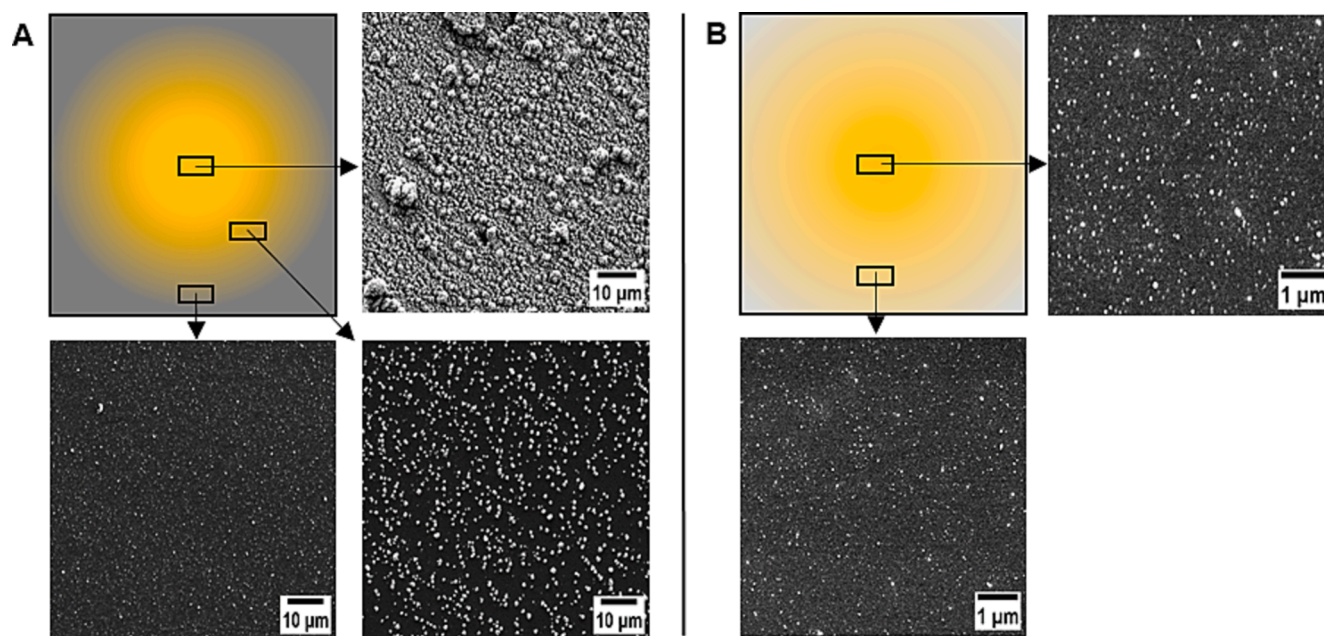


**Fig. 2.** Two sets of SEM images of gold nanoparticles generated by SDG and deposited on a silicon wafer (deposition time: 1000 s) with (A) and without (B) employing the orifice in the impactor. All images were taken with the same magnification. The yellow tinted drawings in each set is only meant to illustrate the overall distribution of the deposited NPs.

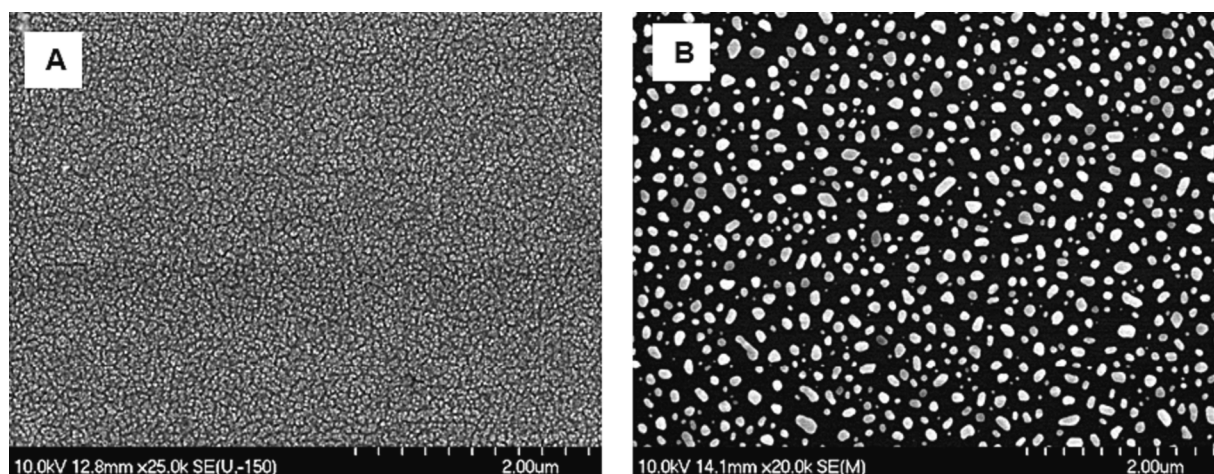


**Fig. 3.** A) Sputtered glass sample coated with gold at 240 s without thermal treatment. B) Sputtered glass sample after thermal treatment for 20 min at 550 °C.

constant across a wide range of deposition times. Thus, overall, the orifice-free SDG-based deposition technique proved to be promising in terms of nanoparticle distribution and morphology.

During magnetron sputtering, highly energetic ions are generated from the ambient noble gas which collide with the gold target thereby ejecting gold atoms. The ejected atoms then diffuse to the solid substrate and condensate, which results in the formation of a film. SEM images of a gold-sputtered substrate (Fig. 3.) show that Au is deposited as a granular structured film at the surface. No singlet NPs can be distinguished, only nanoislands with very little separation between them. This thin film of gold atoms, however, can be converted into quasi-spherical NPs by a 20 min thermal treatment at 550 °C temperature [41]. This is due to the thermal expansion difference between the gold and the substrate that leads to a disaggregation of the film and to the formation of agglomerations due to the relaxation of the thermal stress. This process is not entirely dissimilar to annealing and favors the nucleation and formation of separated gold particles via surface diffusion [42,45]. The size of the produced gold NPs were found to be strongly depending on the sputtering time (thickness, and fell in the range of about 10 to 50 nm in diameter. Generally speaking, sputtering combined with thermal treatment produced the most favourable deposition morphology for NE-LIBS mapping. From this point forward, we always used the thermal treatment after the sputtering, and therefore we will refer to the combined process as sputtering.

### 3.2. Control of surface mass concentration and inter-particle distances

Experimental and theoretical evidence published shows that a 1–3  $\mu\text{g}\cdot\text{cm}^{-2}$  metal surface mass concentration and inter-particle distances (IPDs) comparable to the NP diameter (for efficient plasmon coupling) is needed to optimize the plasmonic effects leading to NE-LIBS signal enhancement [18,20,35]. Therefore we also evaluated the three deposition techniques from the point of view of the control they offer towards IPD and surface concentration.

The surface mass concentration of gold was assessed by performing deposition on a Si substrate masked on all of its sides and the back, only leaving access to a  $10 \times 10$  mm area on the front. Following the deposition, the mask was removed, then the deposited gold was dissolved in aqua regia and the solution was subjected to ICP-MS analysis. Results of this experiment are shown in Fig. 4. As it can be seen, all the three deposition techniques provided a reasonable control of the surface mass concentration simply via the coating (deposition) time. The surface concentration vs. deposition time plots are fairly linear, however clearly the best control of the deposition can be achieved with the sputtering approach. The targeted few  $\mu\text{g}\cdot\text{cm}^{-2}$  mass concentration range can also be achieved with all the three techniques.

The control of particle size obviously would be tightest with the spray coating technique, as this coating process does not change the size

of the particles, if the aggregation/pattern formation would not be that strong. The aggregation also renders any estimations of the IPD mute. Thus, however the coating process does not impose a thermal stress on the substrate (which would be the solid sample in an analytical scenario), spray coating was found to be not suitable for sample preparation prior to NE-LIBS mapping.

During spark discharge-based deposition with the orifice, we found that the IPD decreased from 62.2 nm to 30.0 nm in the center of the substrate as the deposition time was increased from 250 to 2000 s. As it was alluded to it in the former chapter, the particle diameter remained a constant 22 nm throughout the experiments, therefore, by the optimal IPD and particle size relationship can theoretically be achieved with SDG over a small area. A homogenous deposition could only be achieved without the orifice, although at the expense of an impractically long deposition time (e.g. over 60 min). It also has to be mentioned that the coating of large samples (several  $\text{cm}^2$ ) can be problematic with SDG. There is no thermal load on the sample though.

In case of sputtering, the coating time does influence the particle size and the IPD. Our experiments revealed that with increasing coating times the NP size and IPD increased significantly and above 360 s coating time, the shape became irregular. In the 10 to 240 s deposition time range however, the NP diameter increased from 8.87 nm to 51.49 nm (about an eightfold increase) and fairly spherical NPs were obtained. At the 240 s coating time used in all later experiments, the measured mean NP diameter was found to be 51.49 nm and the mean IPD 86.7 nm. This IPD value is well within the critical limit for the NE-LIBS effect to occur [17,18]. An advantage of sputtering is that it can also work with large substrate (sample) surfaces. At the same time the 550 °C thermal post-treatment limits its applicability to heat-resistant samples and also makes the sample preparation lengthier than the actual sputtering. The total duration of coating is still around 24 min, which is acceptable. Overall, the sputtering process was considered to be the most promising of the three deposition techniques, hence we employed this technique during all later experiments.

### 3.3. Laser ablation properties of the sputtered NP layer

In addition to other requirements, the NE-LIBS theory dictates that an as large as possible laser spot size is required to be used, while the fluence is kept in the “LIBS range” (at least some tens of  $\text{J}\cdot\text{cm}^{-2}$ ). This ensures that many, preferably thousands of, nanoparticles are excited jointly with a strong enough electrical field, thereby facilitating an efficient plasmon coupling between them. In practice, millimeter-range spot sizes are common in NE-LIBS, necessitating the use of unusually powerful laser sources, with pulse energies in excess of 100 mJ [17,35]. This disadvantage is somewhat offset in localized NE-LIBS analysis though as it simplifies the NP deposition procedure. This is because pre-shots from the same laser can be used to create an ablation crater of

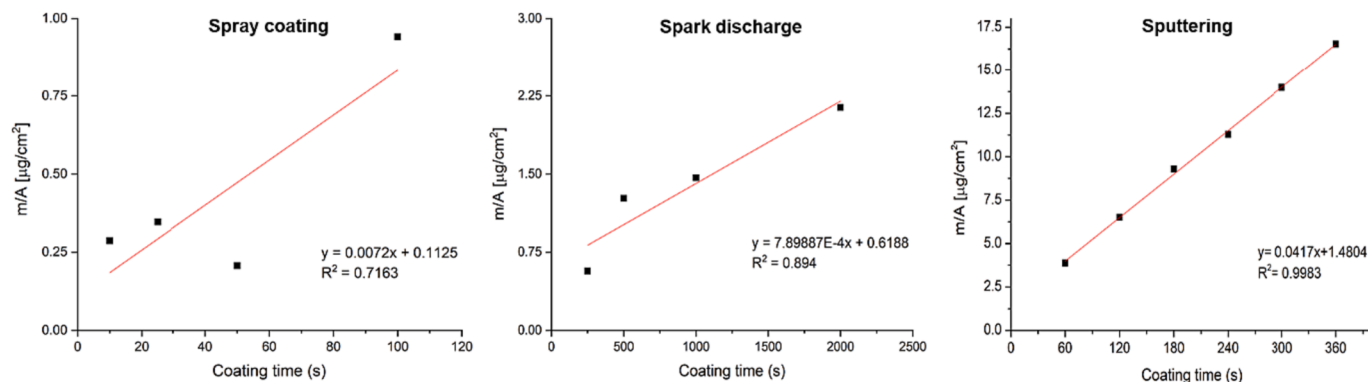


Fig. 4. Control of the overall surface mass concentration of deposited gold NPs by the coating time with various deposition techniques, as quantified by ICP-MS analysis.



sufficient size to aim for when manually pipetting out a small droplet (e.g. 1  $\mu\text{L}$ ) of nanodispersion. This crater will then also help to avoid the spreading of the liquid during the drying step, thereby localizing the NPs [16,18].

However, in elemental mapping, spatial resolution is of primary importance, as many applications require tens of micrometer details to be resolved. Maintaining a too large laser focal spot is directly contradicting this. At first, there seems to be a quick workaround: one just needs to use ultra small NPs, so thousands of them still fit in e.g. a 25–50  $\mu\text{m}$  spot. However, this approach can not fully work for a number of reasons, including, but not limited to i) ultra small NPs have far less number of electrons to donate for plasmons and to provide for the ignition of the laser induced breakdown, ii) it is very hard to keep the IPD in the deposit in the couple of nm range, iii) ultra small NPs tend to be less spherical and their size distribution is typically much wider, iv) smaller NPs will get ablated faster therefore detection gate optimization will be very difficult. All these conditions will weaken the effect and hence decrease the signal enhancement significantly. In addition, a too high spatial resolution puts an even more stringent requirement for the homogeneity of the NP deposition process. In conclusion, a compromise needs to be made between spatial resolution, the signal enhancement gained and practicality. In our view, a 100–200  $\mu\text{m}$  spot size can be a reasonable middle point, which can work fairly well with a few tens of nm diameter NPs.

Even with this spot size in mind, and with eligible candidates for a micro-homogeneous NP deposition, the laser ablation behaviour of the NP layer still needs to be investigated before it can be trusted to provide the analyst with a reliable, enhanced elemental map. Obviously, NE-LIBS will not allow the mapping to be executed in the line scan mode so popular in both LA-ICP-MS and LIBS elemental mapping, due to the largely overlapping ablation spots where each preceding shot would make the surface largely devoid of NPs before the next laser shot. Only stepwise mapping, with non-overlapping spots is feasible. Even in this mode, it needs to be experimentally checked if the shockwave from the ablation would sweep away or rearrange some of the deposited NPs loosely bound to the surface, which would directly influence the achievable step size during mapping. For this purpose, we prepared gold NP-coated silicon substrates with the sputtering deposition technique and delivered several, adjacent, various fluence laser shots to this sample and documented the observable changes on the surface by using SEM.

Fig. 5. shows SEM images in several magnifications, about a portion of a single ablation crater and its rim, as well as its immediate surrounding. It can be observed, that the bottom of the crater, as well as the rim mainly contains molten and resolidified, splashed material (Fig. 5b.), typical in nanosecond laser ablation. Further away from the rim, the original NP layer can be seen (Fig. 5c.), which appears to be undisturbed. In between the above two regions, just adjacent to the rim, a narrow band (ring) can be observed that contains discernible NPs, but in a higher surface density than what is present in the undisturbed part

of the surface (Fig. 5a.). The morphology of this band suggests that the plausible assumption that the shockwave propagating outwards from the laser-illuminated spot dislocates the NPs and push them into the adjacent area, thereby increasing their surface concentration locally. The width of the band was estimated to be a couple of tens of  $\mu\text{m}$  under the conditions used in this experiment. Since this increases the spot size affected by the laser ablation, therefore the maximum available spatial resolution in NE-LIBS mapping may be the diameter of the ablation crater with the molten rim, plus the width of the “compressed” NP band. But before an exact measure could be given to the spatial resolution, the effect of multiple laser shots directed to close by areas, as well as the effect of the laser pulse and the laser spot size were also studied.

We varied the laser focal spot size (60 and 200  $\mu\text{m}$ ) and the pulse energy (5, 10 and 15 mJ) and investigated the laser ablation behaviour of the NP layer in a non-overlapping step scanning mapping situation. The series of SEM images give an overview of the results of these experiments in Fig. 6. One of the most striking detail that the images reveal is that the width of the “compressed” or “rearranged” band around the ablation craters is mostly affected by the laser fluence; the width is larger, both relative to the crater diameter and also by absolute terms, for the 60  $\mu\text{m}$  laser spot size. This clearly indicates the action of the shockwave.

Recently Rehman et al. [46] and Wang et al. [47] studied the effect of laser fluence on the non-linear temporal and spatial propagation of the shockwave front during ns laser ablation of solids and it was established that the shockwave velocity scales roughly with the cubic root of the fluence and both the maximum pressure and the propagation distance also increases nonlinearly with the fluence. Based on these relations, the ca. 11-fold higher laser fluence in the 60  $\mu\text{m}$  spot size case is expected to lead to a more than twice as long shockwave propagation distance, which can explain the 2–2.5 times wider ablation-affected zone around the ablation crater compared to the case of the 200  $\mu\text{m}$  spot size. This also explains that for both spot sizes, the width of the compressed band increases with the pulse energy. This finding strongly discourages the use of smaller spot sizes in NE-LIBS mapping, as it makes the achievable spatial resolution several times poorer than the spot diameter. At the same time, the width of the compressed band at the lower fluence settings remains quite small compared to the 200  $\mu\text{m}$  spot diameter (around 20  $\mu\text{m}$ , or 10 % relative). The loss in spatial resolution probably would be still acceptable for about 175  $\mu\text{m}$  spot sizes, which places the estimate for the true spatial resolution at a value not better than 200  $\mu\text{m}$  at these pulse energies. The overall topography of the surface during the step scan is good; there seems to be no carry-over or incremental effect of adjacent laser shots. In conclusion, these experiments indicate that the ablation behaviour of the deposited NP layer seems to be suitable for NE-LIBS stepwise mapping, with 5–15 mJ pulse energies, typical in ns LIBS analysis, if ca. 175–200  $\mu\text{m}$  spot sizes are used.

With respect to “true spatial resolution”, we would also like to make a point. Although it is a general observation in LIBS (which uses much larger laser fluences than LA-ICP-MS) that ablation craters tend to be

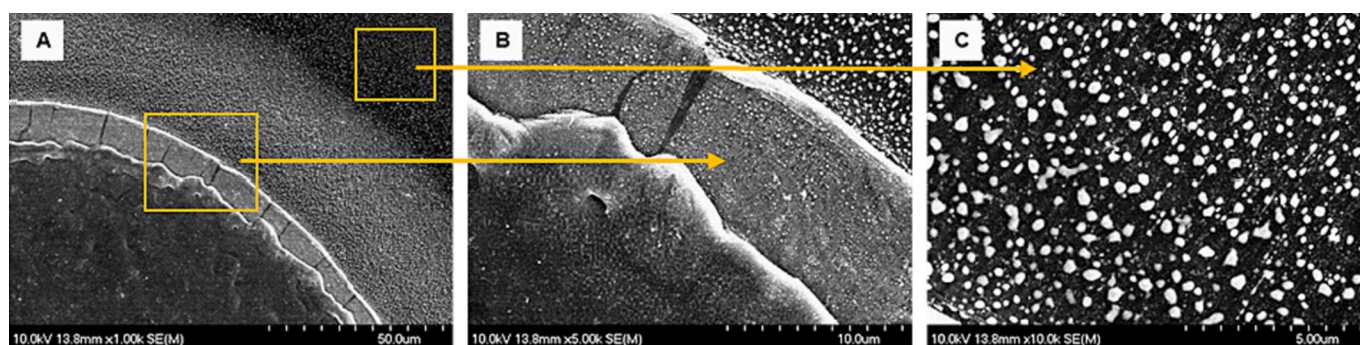
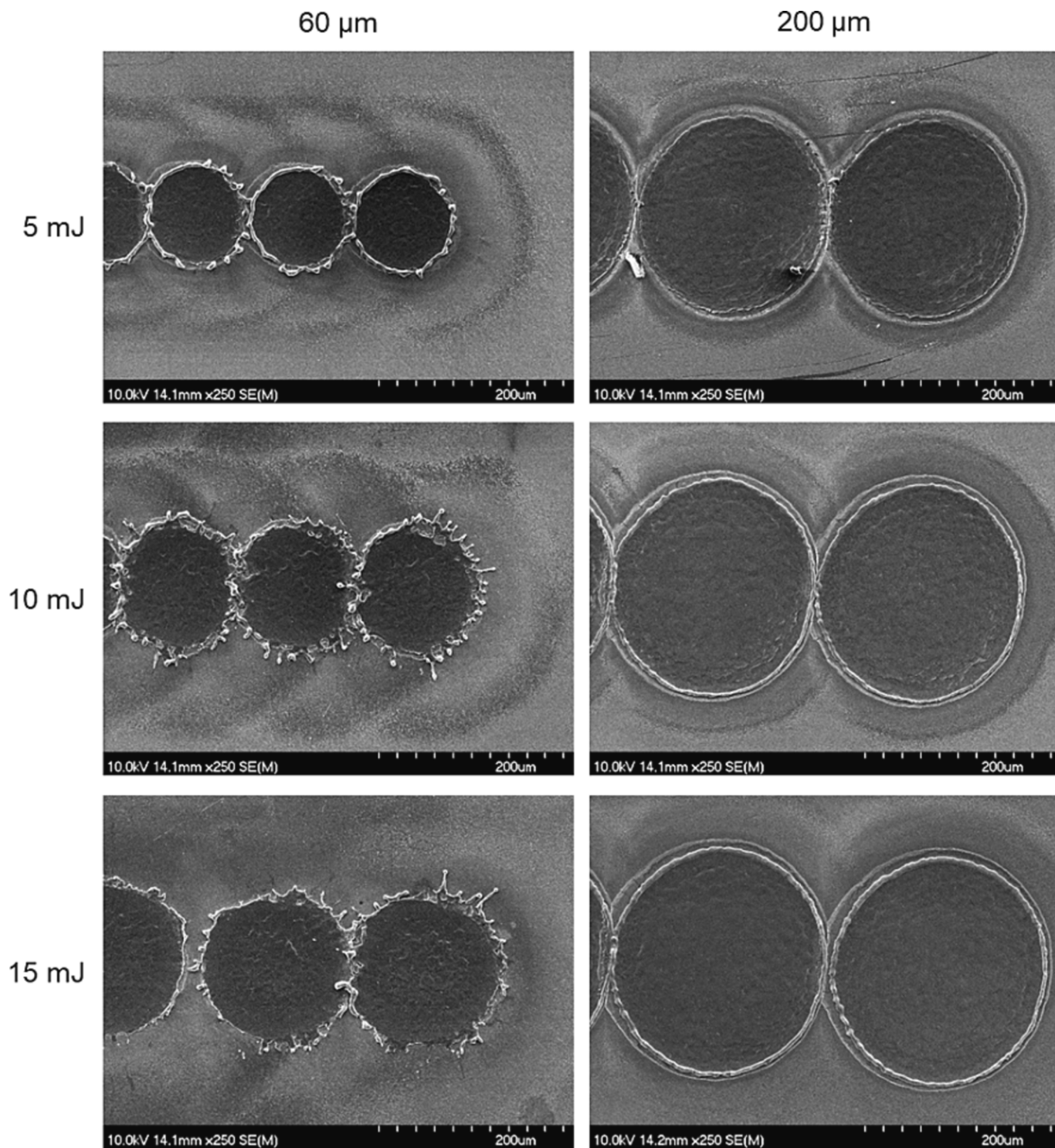


Fig. 5. SEM images of parts of an ablation crater and its surroundings (at different magnifications) produced with a single laser shot on silicon formerly sputter-deposited with gold NPs. Orange frames in image A) indicate the areas that were zoomed in on images B) and C). The laser fluence used was  $31.83 \text{ J}\cdot\text{cm}^{-2}$ .



**Fig. 6.** SEM images of the craters produced using the indicated, different laser pulse energies and laser spot sizes on silicon formerly sputter-deposited with gold NPs. Adjacent images represent laser ablation with about an order of magnitude difference in fluence.

always significantly larger than the optically set laser focal spot diameter, most analysts choose to neglect this effect and report only the set spot diameter (a nice round value, e.g. 25 or 50 or 100  $\mu\text{m}$ ). If the line scan mapping method is used then the overlapping craters disguise this effect anyway, but in reality, only the step scan method provides decent LIBS elemental maps. The step size (true spatial resolution) however needs to be experimentally adjusted to the actual crater size, hence it is always sample- and fluence-dependent. Our above described experiments illustrate such an optimization. In the light of this, the 200  $\mu\text{m}$

spatial resolution estimated is a real and fair value, and this was used in all later part of this study.

In order to test the signal enhancement and its repeatability across a sample surface, stepwise line scans were performed on a glass substrate across a sputter-coated area with gold NPs and the net signal at the Si I 288.15 nm emission line was monitored. The scanned line was longer than the width of the sputtered area, therefore the signal enhancement could also be assessed by using the signal outside the area as reference. Fig. 7. shows the result of this experiment. The graph reveals that a



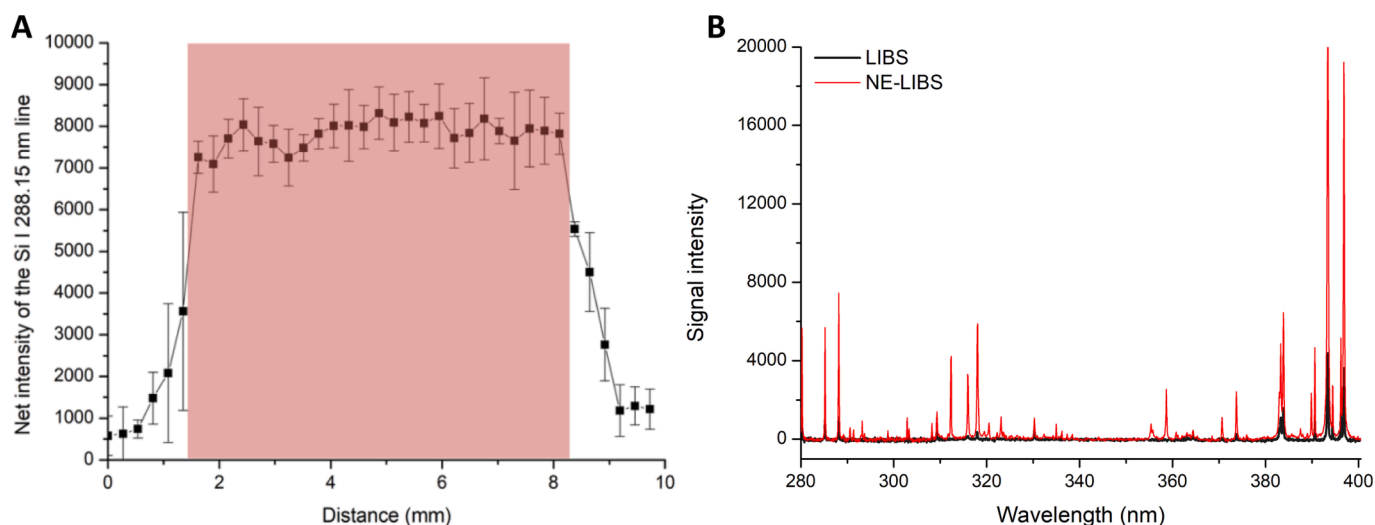


**Fig. 7.** A.) Stepwise line scan on a glass substrate sputtered with gold NPs. The sputtering was limited to the indicated central part (shaded area) by placing a mask with a 6.5 mm opening over the glass substrate in the sputtering device, B.) illustrative glass spectra recorded with NPs (NE-LIBS) and without NPs (LIBS). All conditions are the same as in other experiments reported in this section. Error bars are standard deviations calculated from five repeated measurements.

signal enhancement of about 10 was achieved with integrative detection. The repeatability of the experiment was also good (5–7 % RSD), as is evidenced by the reasonably small error bars obtained from five repetitions. The fact that the signal remained fairly constant over the sputtered area also indicates that the homogeneity of the NP layer is sufficiently good for elemental mapping. Please note that the first and last laser spots were not fully aligned with the edge of the sputtered area, which caused a signal loss at around the edge.

#### 4. Conclusions

We demonstrated that if a proper nanoparticle deposition technique is employed then NE-LIBS mapping is a viable and analytically advantageous approach. We found that out of the three tested deposition techniques the sputter-coating of the solid sample surface with a thin gold layer followed by a thermal treatment at 550 °C that converts the layer into nanoparticles, is a practical and well-controllable NE-LIBS sample preparation approach, at least for samples that are fairly temperature and vacuum stable. The ablation behaviour of the deposited gold NP layer in the LIBS fluence regime was also studied. It was shown that 200  $\mu\text{m}$  spot size is a good compromise between the ideal NE-LIBS conditions and the requirements of chemical mapping.

In comparison with other elemental mapping techniques, such as LA-ICP-MS,  $\mu$ -XRF or even LIBS, the achieved spatial resolution is inferior. However, this resolution is useful in many studies (in the area of e.g. geology, biology, material science or chemistry) already and the use of the NE-LIBS approach does provide substantial benefits in certain analytical scenarios [1,5]. One particular field in which NE-LIBS mapping has a great potential in our opinion is qualitative discrimination, more closely spatial classification/identification of chemical compounds present in a solid sample. Such studies with using classical LIBS have been already performed successfully for e.g. polymers [48], biological tissues [27] or art pieces [49] but the use of the NE-LIBS approach can boost the signal-to-noise ratio of the spectra and this can potentially transform into a better classification accuracy. At present, we are performing these experiments in our laboratory for some industrially relevant sample types.

#### CRediT authorship contribution statement

**F.A. Casian-Plaza:** . **P.M. Janovszky:** . **D.J. Palásti:** . **A. Kohut:** Investigation, Funding acquisition. **Zs. Geretovszky:** Supervision,

Resources. **J. Kopniczky:** Resources, Investigation. **F. Schubert:** Resources, Investigation. **S. Živković:** . **Z. Galbács:** Resources, Methodology. **G. Galbács:** Writing – review & editing, Writing – original draft, Validation, Supervision, Methodology, Funding acquisition, Conceptualization.

#### Declaration of competing interest

The authors declare that they have no known competing financial interests or personal relationships that could have appeared to influence the work reported in this paper.

#### Data availability

Data will be made available on request.

#### Acknowledgements

The authors gratefully acknowledge the financial support from the National Research, Development and Innovation Office (NKFIH) of Hungary through TKP2021-NVA-19, 2019-2.1.11-TÉT-2020-00236, K 146733, PD 139077 and the Nanoplasmonic Laser Fusion Research Laboratory (NAPLIFE) under No. 2022-NL-2.1.1.-2022-00002. Fernando Casian-Plaza also kindly acknowledges financial support from the Consejo Nacional de Humanidades, Ciencias y Tecnologías (CON-AHCYT) of Mexico through project No. 809802. S. Živković thanks for the financial support from the Ministry of Science, Technological Development, and Innovation of the Republic of Serbia (No. 451-03-47/2023-01/200017).

#### References

- [1] G. Galbács, A critical review of recent progress in analytical laser-induced breakdown spectroscopy, *Anal. Bioanal. Chem.* 407 (2015) 7537–7562, <https://doi.org/10.1007/s00216-015-8855-3>.
- [2] D.W. Hahn, N. Omenetto, Laser-induced breakdown spectroscopy (LIBS), part II: review of instrumental and methodological approaches to material analysis and applications to different fields, *Appl. Spectrosc.* 66 (4) (2012) 347–419, <https://doi.org/10.1366/11-06574>.
- [3] D.F. Andrade, E.R. Pereira-Filho, D. Amarasiriwardena, Current trends in laser-induced breakdown spectroscopy: a tutorial review, *Appl. Spectrosc. Rev.* 56 (2021) 98–114, <https://doi.org/10.1080/05704928.2020.1739063>.
- [4] A.A. Bol'shakov, X. Mao, J.J. González, R.E. Russo, Laser ablation molecular isotopic spectrometry (LAMIS): current state of the art, *J. Anal. at. Spectrom.* 31 (2016) 119–134, <https://doi.org/10.1039/C5JA00310E>.



- [5] A. Limbeck, L. Brunnbauer, H. Lohninger, P. Pořízka, P. Modlitbová, J. Kaiser, P. Janovszky, A. Kéri, G. Galbács, Methodology and applications of elemental mapping by laser induced breakdown spectroscopy, *Anal. Chim. Acta.* 1147 (2021) 72–98, <https://doi.org/10.1016/j.aca.2020.12.054>.
- [6] G. Galbács, Laser-induced breakdown spectroscopy, in *biological, forensic and materials sciences*, first ed., Springer Nature, Switzerland, 2022.
- [7] J.P. Singh, S.N. Thakur, Laser-induced breakdown spectroscopy, second ed., Elsevier, 2020.
- [8] A.W. Miziolek, V. Palleschi, I. Schechter, Laser-induced breakdown spectroscopy (LIBS): fundamentals and applications, second ed., Cambridge University Press, 2009.
- [9] D.A. Cremers, L.J. Radziemski, Handbook of laser-induced breakdown spectroscopy, first ed., John Wiley and Sons, 2013.
- [10] V.K. Singh, D.K. Tripathi, Y. Deguchi, Z. Wang, Laser induced breakdown spectroscopy (LIBS): concepts, instrumentation, data analysis and applications, first ed., Wiley and Sons, 2023.
- [11] S. Musazzi, U. Perini, Laser-induced breakdown spectroscopy: theory and applications, first ed., Springer, Berlin, Heidelberg, 2014.
- [12] R. Noll, Laser-induced breakdown spectroscopy, fundamentals and applications, first ed., Springer, Berlin, Heidelberg, 2012.
- [13] Y. Li, D. Tian, Y. Ding, G. Yang, K. Liu, C. Wang, X. Han, A review of laser-induced breakdown spectroscopy signal enhancement, *Appl. Spectrosc. Rev.* 53 (2018) 1–35, <https://doi.org/10.1080/05704928.2017.1352509>.
- [14] G. Galbács, D.J. Palásti, P.M. Janovszky, State-of-the-art analytical performance, in: G. Galbács (Ed.), *Laser-Induced Breakdown Spectroscopy, in Biological, Forensic and Materials Sciences*, Springer Nature, Switzerland, 2022, pp. 101–127.
- [15] T. Ohta, M. Ito, T. Kotani, T. Hattori, Emission enhancement of laser-induced breakdown spectroscopy by localized surface plasmon resonance for analyzing plant nutrients, *Appl. Spectrosc.* 63 (2009) 555–558, <https://doi.org/10.1366/000370209788346896>.
- [16] A. De Giacomo, R. Gaudioso, C. Koral, M. Dell'Aglio, O. De Pascale, Nanoparticle-enhanced laser-induced breakdown spectroscopy of metallic samples, *Anal. Chem.* 85 (21) (2013) 10180–10187, <https://doi.org/10.1021/ac4016165>.
- [17] M. Dell'Aglio, R. Alrifai, A. De Giacomo, Nanoparticle enhanced laser induced breakdown spectroscopy (NELIBS), a first review, *Spectrochim. Acta B.* 148 (2018) 105–112, <https://doi.org/10.1016/j.sab.2018.06.008>.
- [18] A. De Giacomo, M. Dell'Aglio, R. Gaudioso, C. Koral, G. Valenza, Perspective on the use of nanoparticles to improve LIBS analytical performance: nanoparticle enhanced laser induced breakdown spectroscopy (NELIBS), *J. Anal. at. Spectrom.* 31 (2016) 1566–1573, <https://doi.org/10.1039/C6JA00189K>.
- [19] G. Galbács, A. Kéri, A. Kohut, M. Veres, Zs. Geretovszky, Nanoparticles in analytical laser and plasma spectroscopy – a review of recent developments in methodology and applications, *J. Anal. at. Spectrom.* 36 (2021) 1826–1872, <https://doi.org/10.1039/D1JA00149C>.
- [20] A. De Giacomo, R. Gaudioso, C. Koral, M. Dell'Aglio, O. De Pascale, Nanoparticle enhanced laser induced breakdown spectroscopy: effect of nanoparticles deposited on sample surface on laser ablation and plasma emission, *Spectrochim. Acta B.* 98 (2014) 19–27, <https://doi.org/10.1016/j.sab.2014.05.010>.
- [21] D.J. Palásti, P. Albrycht, P. Janovszky, K. Paszkowska, Z. Geretovszky, G. Galbács, Nanoparticle enhanced laser induced breakdown spectroscopy of liquid samples by using modified surface-enhanced Raman scattering substrates, *Spectrochim. Acta B.* 166 (2020) 105793, <https://doi.org/10.1016/j.sab.2020.105793>.
- [22] J. Shen, K. Wu, D. Cao, J. Wang, B. Hu, Effect of Ag nanoclusters deposited with magnetron sputtering on laser-induced breakdown spectroscopy enhancement, *Spectrochim. Acta B.* 156 (2019) 59–65, <https://doi.org/10.1016/j.sab.2019.05.001>.
- [23] H. Qayyum, R. Ali, Z.U. Rehman, S. Ullah, B. Shafique, A.H. Dogar, A. Shah, A. Qayyum, Synthesis of silver and gold nanoparticles by pulsed laser ablation for nanoparticle enhanced laser-induced breakdown spectroscopy, *J. Laser Appl.* 31 (2) (2019) 022014, <https://doi.org/10.2351/1.5086838>.
- [24] L. Jolivet, M. Leprince, S. Moncayo, L. Sorbier, C.-P. Lienemann, V. Motto-Ros, Review of the recent advances and applications of LIBS-based imaging, *Spectrochim. Acta B.* 151 (2019) 41–53, <https://doi.org/10.1016/j.sab.2018.11.008>.
- [25] V. Pinon, M.P. Mateo, G. Nicolas, Laser-induced breakdown spectroscopy for chemical mapping of materials, *Appl. Spectrosc. Rev.* 48 (2013) 357–383, <https://doi.org/10.1080/05704928.2012.717569>.
- [26] V.K. Singh, N. Sharma, O.N. Verma, V.K. Singh, D.K. Tripathi, Y. Lee, S. Kumar, P. K. Rai, M.A. Gondal, Review: Application of LIBS to elemental analysis and mapping of plant samples, *At. Spectrosc.* 42 (2021) 99–113, [10.46770/AS.2020.20](https://doi.org/10.46770/AS.2020.20).
- [27] P. Janovszky, A. Kéri, D.J. Palásti, L. Brunnbauer, F. Domoki, A. Limbeck, G. Galbács, Quantitative elemental mapping of biological tissues by laser-induced breakdown spectroscopy using matrix recognition, *Sci. Rep.* 13 (2023) 10089, <https://doi.org/10.1038/s41598-023-37258-y>.
- [28] P. Janovszky, K. Jancsek, D.J. Palásti, J. Kopniczky, B. Hopp, T.M. Tóth, G. Galbács, Classification of minerals and the assessment of lithium and beryllium content in granitoid rocks by laser-induced breakdown spectroscopy, *J. Anal. at. Spectrom.* 36 (2021) 813–823, <https://doi.org/10.1039/D1JA00032B>.
- [29] M. Weiss, Z. Gajarska, H. Lohninger, M. Marchetti-Deschmann, G. Ramer, B. Lendl, A. Limbeck, Elemental mapping of fluorine by means of molecular laser induced breakdown spectroscopy, *Anal. Chim. Acta.* 1195 (2022) 339422, <https://doi.org/10.1016/j.aca.2021.339422>.
- [30] A.A. Khedr, M.A. Sliem, M. Abdel-Harith, Gold nanoparticle-enhanced laser-induced breakdown spectroscopy and three-dimensional contour imaging of an aluminum alloy, *Appl. Spectrosc.* 75 (2021) 565–573, <https://doi.org/10.1177/0003702820973040>.
- [31] Z. Xiande, C. Zhao, D. Xiaofan, D. Daming, Detecting and mapping harmful chemicals in fruit and vegetables using nanoparticle-enhanced laser-induced breakdown spectroscopy, *Sci. Rep.* 9 (2019) 906, <https://doi.org/10.1038/s41598-018-37556-w>.
- [32] M. Holá, Z. Salajková, A. Hrdlička, P. Pořízka, K. Novotný, L. Čelko, P. Šperka, D. J. Novotný, P. Modlitbová, V. Kanický, J. Kaiser, Feasibility of nanoparticle-enhanced laser ablation inductively coupled plasma mass spectrometry, *Anal. Chem.* 90 (2018) 11820–11826, <https://doi.org/10.1021/acs.analchem.8b01197>.
- [33] M. Holá, Z. Salajková, A. Hrdlička, J. Ondráček, K. Novotný, D. Pavlínek, M. Vojtěšek-Lom, L. Čelko, P. Pořízka, V. Kanický, D. Procházka, J. Novotný, J. Kaiser, The effect of nanoparticle presence on aerosol formation during nanoparticle-enhanced laser ablation inductively coupled plasma mass spectrometry, *J. Anal. at. Spectrom.* 35 (2020) 2893–2900, <https://doi.org/10.1039/D0JA00324G>.
- [34] A. Mangone, F. Mastroiocco, L.C. Giannossa, R. Comparelli, M. Dell'Aglio, A. De Giacomo, Nanoparticle enhanced laser ablation inductively coupled plasma mass spectrometry, *Spectrochim. Acta B.* 163 (2020) 105731, <https://doi.org/10.1016/j.sab.2019.105731>.
- [35] Z. Salajková, V. Gardette, J. Kaiser, M. Dell'Aglio, A. De Giacomo, Effect of spherical gold nanoparticles size on nanoparticle enhanced laser induced breakdown spectroscopy, *Spectrochim. Acta B.* 179 (2021) 106105, <https://doi.org/10.1016/j.sab.2021.106105>.
- [36] T. Takahashi, B. Thornton, Quantitative methods for compensation of matrix effects and self-absorption in laser induced breakdown spectroscopy signals of solids, *Spectrochim. Acta B.* 138 (2017) 31–42, <https://doi.org/10.1016/j.sab.2017.09.010>.
- [37] M. Martínez, M. Baudelet, Calibration strategies for elemental analysis of biological samples by LA-ICP-MS and LIBS – a review, *Anal. Bioanal. Chem.* 412 (2020) 27–36, <https://doi.org/10.1007/s00216-019-02195-1>.
- [38] L.P. Villy, A. Kohut, A. Kéri, Á. Bélteki, Gy. Radnóczy, Zs. Fogarassy, Gy. Z. Radnóczy, G. Galbács, Zs. Geretovszky, Continuous spark plasma synthesis of Au/Co binary nanoparticles with tunable properties, *Sci. Rep.* 12 (2022) 18560, <https://doi.org/10.1038/s41598-022-22928-0>.
- [39] A. Kohut, L.P. Villy, A. Kéri, Á. Bélteki, D. Megyeri, B. Hopp, G. Galbács, Zs. Geretovszky, Full range tuning of the composition of Au/Ag binary nanoparticles by spark discharge generation, *Sci. Rep.* 11 (1) (2021) 5117, <https://doi.org/10.1038/s41598-021-84392-6>.
- [40] D.J. Palásti, L. Villy, B. Leits, A. Kéri, A. Kohut, Á. Bélteki, Gy. Kajner, F.A. Casian Plaza, É. Kovács-Széles, T. Ajtai, M. Veres, Zs. Geretovszky, G. Galbács, Detection and characterization of mono- and bimetallic nanoparticles produced by electrical discharge plasma generators using laser-induced breakdown spectroscopy, *Spectrochim. Acta B.* 209 (2023) 106804, <https://doi.org/10.1016/j.sab.2023.106804>.
- [41] A. Bonyár, I. Csarnovics, M. Veres, L. Himics, A. Csik, J. Kámán, L. Balázs, S. Kökényesi, Investigation of the performance of thermally generated gold nanoislands for LSPR and SERS applications, *Sens. Actuators B: Chem.* 255 (2018) 433–439, <https://doi.org/10.1016/j.snb.2017.08.063>.
- [42] C. Worsch, W. Wisniewski, M. Kracker, C. Rüssel, Gold nano-particles fixed on glass, *Appl. Surf. Sci.* 258 (22) (2012) 8506–8513, <https://doi.org/10.1016/j.apsusc.2012.05.010>.
- [43] R.D. Deegan, O. Bakajin, T.F. Dupont, G. Huber, S.R. Nagel, T.A. Witten, Contact line deposits in an evaporating drop, *Phys. Rev. E.* 62 (1) (2000) 756, <https://doi.org/10.1103/PhysRevE.62.756>.
- [44] M.V. Rukosuyev, O. Barannyk, P. Oshkay, M.B. Jun, Design and application of nanoparticle coating system with decoupled spray generation and deposition control, *J. Coat. Technol. Res.* 13 (5) (2016) 769–779, <https://doi.org/10.1007/s11998-016-9788-2>.
- [45] A. Serrano, O. Rodriguez de la Fuente, M.A. García, M. A. Extended and localized surface plasmons in annealed Au films on glass substrates, *J. Appl. Phys.* 108 (7) (2010) 074303, [10.1063/1.3485825](https://doi.org/10.1063/1.3485825).
- [46] Z.U. Rehman, A. Raza, H. Qayyum, S. Ullah, S. Mahmood, A. Qayyum, Characterization of laser-induced shock waves generated during infrared laser ablation of copper by the optical beam deflection method, *Appl. Opt.* 61 (2022) 8606–8612, <https://doi.org/10.1364/AO.472340>.
- [47] Y. Wang, C. Liu, C. Li, Evolution of ns pulsed laser induced shock wave on aluminum surface by numerical simulation, *Results Phys.* 22 (2021) 103920, <https://doi.org/10.1016/j.rinp.2021.103920>.
- [48] L. Brunnbauer, S. Larisegger, H. Lohninger, M. Nelhiebel, A. Limbeck, Spatially resolved polymer classification using laser induced breakdown spectroscopy (LIBS) and multivariate statistics, *Talanta.* 209 (2020) 120572, <https://doi.org/10.1016/j.talanta.2019.120572>.
- [49] L. Pagnin, L. Brunnbauer, R. Wiesinger, A. Limbeck, M. Schreiner, Multivariate analysis and laser-induced breakdown spectroscopy (LIBS): a new approach for the spatially resolved classification of modern art materials, *Anal. Bioanal. Chem.* 412 (2020) 3187–3198, <https://doi.org/10.1007/s00216-020-02574-z>.